Effect of the molding conditions on mode II interlaminar crack propagation in continous glass fiber/polypropylene composites

Bureau, M. N.; Denault, J.; Dickenson, J. I.

Publisher's version / Version de l'éditeur:

Series (National Research Council of Canada. Industrial Materials Institute); no. IMI2001-87973-G, 2001

IMI2001-87973-G CNRC 44553

EFFECT OF THE MOLDING CONDITIONS ON MODE II INTERLAMINAR CRACK PROPAGATION IN CONTINUOUS GLASS FIBER/POLYPROPYLENE COMPOSITES

M. N. BUREAU*[1], J. DENAULT* AND J. I. DICKSON**

**Industrial Materials Institute, National Research Council Canada*

75, de Mortagne, Boucherville (Canada) J4B 6Y4 (martin.bureau@nrc.ca; 450-641-5179)

*** École Polytechnique, Montreal (Canada), C. P. 6079, Succ. Centre-Ville, H3C 3A7*

SUBMITTED TO JTCM 2000-63

REVISED VERSION

---

[1] To whom correspondence should be addressed.

EFFECT OF THE MOLDING CONDITIONS ON MODE II INTERLAMINAR CRACK PROPAGATION IN CONTINUOUS GLASS FIBER/POLYPROPYLENE COMPOSITES

M. N. BUREAU*[2], J. DENAULT* AND J. I. DICKSON**

**Industrial Materials Institute, National Research Council Canada*

75, de Mortagne, Boucherville (Canada) J4B 6Y4 (martin.bureau@nrc.ca; 450-641-5179)

*** École Polytechnique, Montreal (Canada), C. P. 6079, Succ. Centre-Ville, H3C 3A7*

ABSTRACT

The effect of molding conditions on the resistance to mode II interlaminar crack propagation under monotonic and cyclic loading of unidirectional continuous glass fiber composites with a polypropylene (PP) matrix was studied. The distribution of the fibers and of the crystalline and amorphous components of the matrix phase, the melting temperature and the amount of crystallinity are related to the molding conditions employed and to the resulting flexural strength and modulus, apparent interlaminar shear strength and Young's modulus. Mode II crack propagation, either cyclic or monotonic, is strongly affected by the fiber-matrix interface and matrix morphology. The distribution of the soft amorphous PP phase in the semi-crystalline PP matrix appears to be the controlling parameter determining the fracture and fatigue resistance of the composite. The fractographic features clearly show the role that this phase plays during crack propagation. A relationship between the shear cusp size measured on the fatigue surfaces and the cyclic strain energy release rate is proposed.

KEY WORDS: Continuous Glass Fiber/Polypropylene Composite, Fracture, Fatigue, Interlaminar Crack Propagation

Martin N. Bureau is a research officer at the *Industrial Materials Institute (IMI)* of the *National Research Council Canada (NRC)* in the Polymer Composite group. He graduated in 1992 in Metallurgical Engineering at École Polytechnique (Montreal). His Ph. D. thesis on Fatigue Crack Propagation of Thermoplastic Polymer Blends was co-supervised by Prof. John Ivan Dickson at École Polytechnique and Dr. Johanne Denault from NRC-IMI.

---

[2] To whom correspondence should be addressed.

EFFECT OF THE MOLDING CONDITIONS ON MODE II INTERLAMINAR CRACK PROPAGATION IN CONTINUOUS GLASS FIBER/POLYPROPYLENE COMPOSITES

INTRODUCTION

Continuous glass fiber/polypropylene (glass/PP) composites have been extensively studied recently due to their low production cost (less expensive raw materials, faster molding processes, possibilities of automation, etc.) combined with their high damage tolerance, high chemical and environment resistance and recyclability. Results obtained in these composites (1-5) however revealed that the thermal history of the molded part (as influenced by the molding temperature, holding time, cooling rate and post-processing heat treatment) has a critical impact in determining its mechanical behavior.

By varying the cooling rate or the crystallization time during the molding process of glass/PP composites, the mode I interlaminar fracture toughness was shown to vary by as much as 400% (1) and the interlaminar shear strength by 175% (3). This variation was shown to depend on the resulting degree of crystallinity, crystalline-amorphous phase configuration and fiber-matrix adhesion. For the same cooling histories, the mode II interlaminar fracture toughness did not show such a significant variation (2). As presented earlier (4), the fatigue life diagram of the glass/PP composite studied presents a progressive damage region, indicative of the initiation, propagation and coalescence of microstructural damage (6,7), controlled essentially by the occurrence of local delamination under interlaminar shear stresses associated with transverse cracks (8). While it is recognized that the processing strongly affects the mechanical behavior of glass/PP composites, its effect on mode II fatigue crack propagation has not been specifically addressed.

The objective of the present study is to investigate the role of the molding conditions on the microstructure and crystalline/amorphous phase configuration of a unidirectional glass/PP composite and to evaluate their effect on the mechanical properties. The interlaminar fracture behavior of this composite, as indicated by its mode II interlaminar subcritical crack propagation curve and its fractography, is compared to its interlaminar fatigue behavior to understand the mechanisms leading to failure by delamination in glass composites with a ductile thermoplastic matrix.

EXPERIMENTAL

Material Preparation

The composite studied was fabricated from unidirectional pre-impregnated 0.5-mm thick tapes, supplied by Baycomp Canada, which had 60 wt.% of continuous E-glass fibers. According to the supplier, the glass fibers were silane-treated to ensure optimum fiber-matrix interfacial strength. The PP matrix consisted of an impact-modified PP blend with a chemically modified PP. Unidirectional glass/PP composites were prepared from 8 layers of tape under three different compression molding conditions. These conditions are described in Table 1 and will be referred to as the normal molding condition (NM), the slow cooling condition (SC) and the low temperature molding condition (LTM). Compression molding was done employing a Wabash press in a steel closed-mold under a pressure of 0.69 MPa maintained during cooling until the end of the crystallization process was reached (generally below 100°C). A holding time of 5 minutes was employed for the NM and SC conditions since good impregnation and consolidation were rapidly obtained at 200°C (3). In the LTM condition, however, the holding time was increased to 20 minutes to compensate for the reduced matrix viscosity at 163°C, slowing down the impregnation and consolidation kinetics (3). The resulting fiber fraction in the glass/PP composite was 60 wt.% or 35 vol.% for each of the molding conditions studied.

Microscopic and Calorimetric Techniques

A permanganate chemical etching technique (9) was employed on pre-polished surfaces to reveal the microstructure of the PP matrix of the composite. This technique involved immersion for 30 min in a solution composed of 0.7 g of potassium permanganate ($KMnO_4$) in 35 ml of concentrated phosphoric acid (H_3PO_4) and 65 ml of sulfuric acid (H_2SO_4). Intensive washing with a solution of 30 ml of sulfuric acid in 70 ml of distilled water, with hydrogen peroxide (H_2O_2), distilled water and acetone was employed to remove any remaining contamination artifacts from the etched surfaces followed the etching procedure. The microstructure of the PP matrix was observed using a JEOL JSM-6100 scanning electron microscope (SEM). Image analysis was employed to measure the size distribution of the crystalline phase. All specimens observed in the SEM were first coated with a thin layer of gold-palladium.

The melting characteristics of the PP matrix in the glass/PP composite were obtained employing a Perkin-Elmer differential scanning calorimeter (DSC-7) with a scanning rate of 20°C/min. The DSC samples were sectioned from the middle of the molded plates. After the DSC scans, the samples were pyrolized at 450°C for 2 hours to obtain the

resin weight fraction in each sample analyzed. The apparent degree of crystallinity, X_c, was calculated from the heat of fusion of pure fully crystalline isotactic PP, ΔH_f^o, of 207 J/g (10) and the following equation:

$$X_c = \frac{\Delta H_f}{(1 - W_f)\Delta H_f^o} \tag{1}$$

where W_f is the resin weight fraction and ΔH_f is the heat of fusion (in J per g of composite) of the samples. Averages of three DSC scans were determined.

Mechanical Testing Techniques

The flexural modulus, the flexural strength and the maximum strain in the outer fibers of the glass/PP composite were obtained following the ASTM D-790M standard test method. These tests were performed at room temperature using a three-point bending set-up with a nominal specimen thickness of 4 mm, a span of 51 mm and a crosshead speed of 1.3 mm/min. Young's modulus, which required in the calculation of the compliance, was also obtained according to ASTM D-3039M in the different molding conditions. Five or more specimens were tested in three-point bending and in tension. The standard deviation of the reported average values is 5% or less.

The apparent interlaminar shear strength of the glass/PP composite was determined using the short-beam method according to ASTM D-2344M. The nominal specimen thickness was 4 mm, the support span 20 mm and the crosshead speed 1.3 mm/min. Interlaminar shear fracture of the short-beam shear (SBS) specimens could not be obtained at room temperature due to the low rigidity of the PP matrix above its glass transition temperature (near 0°C). Consequently, the short-beam shear (SBS) tests were performed at –40°C in order to obtain valid results. The SBS results thus reflect the interlaminar shear strength of the glass/PP composites at –40°C. Five or more specimens were tested. The standard deviation of the reported average values is 5% or less.

The mode II interlaminar crack propagation tests, both in steady crack growth and in fatigue, were performed at room temperature employing end-notched flexure (ENF) specimens (11), schematized in Fig. 1. This specimen is essentially a three-point bending specimen with an imbedded through-width delamination crack present at one end. The purpose of this test is to determine the strain energy release rate, G_{II}, associated with interlaminar cracking in pure mode II loading. The ENF specimen has been found to produce shear loading at the crack tip without

introducing excessive friction between the crack surfaces (12). A polyethylene terephthalate (PET) film, 20 μm in thickness, was inserted at mid-thickness into the plates prior to molding in order to generate an initial crack. The nominal specimen thickness, 2h, was 4 mm, the specimen width, w, was 20 mm, the specimen length was 130 mm and the total span, 2L, was 110 mm. A restraining bar on the side opposite to the initial interlaminar crack (Fig. 1) was employed to prevent any movement of the specimen that might result from its unsymmetrical deflection during the crack propagation tests.

The crack length of the ENF specimens, a, was monitored during monotonic and cyclic loading using the compliance calibration method (12). The compliance, C, was measured at 5-mm crack length increments from 0 to 55 mm (i.e. from a/L = 0 to 1.0) on the initial linear portion of the load-deflection curve of the ENF specimens under the same loading conditions mentioned below for the fracture and fatigue tests. As given by the beam theory (11), the compliance expression of the ENF specimen is:

$$C = \frac{2L^3 + 3a^3}{8Ewh^3} \tag{2}$$

where E is Young's modulus. In the case of good agreement between the measured and calculated values of compliance, the crack length during monotonic and cyclic loading can be obtained from the load-deflection curve employing Eq. 2. The crack length calculated from the compliance calibration at the beginning and at the end of the tests was compared with the crack lengths measured manually with a travelling microscope to verify the accuracy of the crack length calculations. In all cases, the difference between the predicted and measured values was less than 0.5 mm.

The interlaminar fracture tests were performed in monotonic loading under fixed-grip conditions at a constant crosshead speed of 5 mm/min. Five specimens, with an initial crack length, a_0, of 30 mm, were tested for each molding condition. The crack length was monitored during the tests using the compliance calibration method. The crack length was also measured at the beginning and at the end of the tests using a travelling microscope to verify the crack length monitoring. In all cases, the difference between the monitored and measured values was less than 0.5 mm. With the crack length obtained, the mode II strain energy release rate, G_{II}, can be obtained from the load-deflection curves using the following expression:

$$G_{II} = \frac{P^2}{2w}\frac{\partial C}{\partial a} = \frac{9P^2Ca^2}{2w(2L^3 + 3a^3)} \tag{3}$$

Two specific values for the mode II interlaminar fracture resistance are obtained from these curves using Eq. 3: one at the onset of subcritical crack propagation, $G_{IIc,subcritical}$, determined from the point of deviation from the linear portion of the load-deflection curve, and the other at crack instability, $G_{IIc,instability}$, determined from the maximum load on the load-deflection curve (13). The standard deviation of the reported average G_{IIc} values was 10% or less. All ENF specimens were carefully examined to verify that no damage, other than a propagating shear crack at mid-thickness, was produced.

The interlaminar fatigue tests were performed using a computer-controlled servo-hydraulic test machine under constant cyclic loading with a sinusoidal waveform, a cyclic frequency of 5 Hz and a minimum to maximum load ratio of 0.1. Two specimens, each with an initial crack length of 24.5 mm, were tested for each molding condition. These specimens were precracked in fatigue until a minimum crack length of 26 mm was obtained to avoid compressive forces between the crack faces near the lateral load point resulting in artificially high crack propagation resistance. A maximum fatigue crack length of 51 mm was also employed to minimize the influence of sliding friction on crack propagation attributed to the compressive stress field near the center load point. These crack requirements as well as the approach chosen for the interlaminar fatigue tests were obtained from the modification of the beam theory for ENF specimens under cyclic loading (12). The load-deflection curves were saved at regular fatigue cycle increments. The crack length was calculated from the slope of the first linear portion of the load-increasing curves employing the cyclic compliance calibration. Each fatigue propagation data point was obtained over a minimum crack propagation distance of 0.2 mm, as recommended in the ASTM E-647 standard test method. The crack length was also measured at the beginning of and during the tests using a travelling microscope to verify the crack length monitoring by the compliance method. In all cases, the difference between the monitored and measured values was less than 0.5 mm. The fatigue crack growth rate, da/dN, where N is the number of cycles, was calculated for the crack length calculations. The corresponding mode II strain energy release rate amplitude, ΔG_{II}, was obtained from Eq. 3 using the fixed load amplitude, ΔP, given by $P_{max} - P_{min}$, where P_{max} was under the load leading to unstable fracture until the end of the fatigue tests. The fatigue crack propagation behavior is expressed as log-log curves of da/dN *vs.* ΔG_{II}.

RESULTS AND DISCUSSION

Calorimetry and Microscopy

SEM micrographs of the etched pre-polished surface of the glass/PP composites in the different molding conditions are presented in Fig. 2 at high magnification to show the morphology of the matrix. In the NM and SC conditions, both with a molding temperature of 200°C, a spherulitic crystalline structure is obtained, as shown in Fig. 2a and 2b. These micrographs also show that the SC condition results in marked spherulite boundaries often presenting large gaps between individual spherulites (Fig. 2b); whereas, the NM condition results in considerably less-marked interspherulitic regions (Fig. 2a). The marked spherulite boundaries, in some cases localized interspherulitic cracking, are the result of the slow crystallization process, during which more non-crystallizable PP material, such as low molecular weight macromolecules and impurities, is rejected from the crystallization front (14). This leads to low amounts of amorphous phase and of tie-molecules in the interspherulitic regions, often resulting in local voids. Increased dissolution by the permanganate chemical etching of the non-crystalline and less chemical resistant interspherulitic regions may also increase the apparent size of these voids. In the LTM condition, however, the crystalline structure is not clear (Fig. 2c), as a result of the low molding temperature, with only immature spherulites occasionally observed, and the fiber dispersion is poor, as a result of the high matrix viscosity obtained during molding. In the three conditions, the presence is noted of a large number of regularly distributed voids generally well under 0.5 μm in diameter and probably corresponding to the impact modifier added to PP.

Image analysis was performed to measure the size of the spherulites in the NM and SC conditions. As shown in Fig. 3, a normal distribution of the spherulite size is observed in both conditions. For the NM condition, the average spherulite size measured is 26 μm and the maximum spherulite size is 40 μm. For the SC condition, the average spherulite size measured is 34 μm and the maximum spherulite size is 60 μm. These results are shown in Table 2. Due to the difficulty of observing a clear crystalline structure in the LTM condition, quantitative measurements could not be performed. When discernible, crystalline phase domains approximately 10 μm in diameter were observed. It can thus be considered that the average size of the crystalline structure is considerably lower in the LTM condition than in the other two conditions.

Differential scanning calorimetry was employed to characterize the crystalline microstructure of the PP matrix obtained under the different molding conditions. A DSC heating scan is shown in Fig. 4 for each molding condition. The temperature at the peak of fusion and the degree of crystallinity obtained from the DSC scans are reported in Table 2. These results indicate that, as the cooling rate is reduced, the endothermic melting peak is moved to higher temperatures, suggesting that higher thermal stability of the crystalline phase is obtained, in agreement with the increased spherulite size. However, the same degree of crystallinity of 44% is obtained for both NM and SC conditions. The results in Fig. 4 and Table 2 also indicate that in the LTM condition the degree of crystallinity is slightly higher at 49%, the melting temperature at the maximum of the endothermic peak of fusion increases significantly by 8 to 10°C at 170°C and the average size of spherulites strongly decreases to a value below 10 μm.

From the SEM and DSC results, it can be concluded that spherulites of larger size with sharper boundaries and with higher melting temperatures are obtained when lower cooling rates are employed. In the range tested, however, the reduction in cooling rate does not affect the degree of crystallinity. This differs from the reported variation in the degree of crystallinity from 52% at high cooling rates (similar to the NM condition) to 66% at low cooling rates (similar to the SC condition) reported for other glass/PP composites (1). This lack of effect of cooling rate variations on the degree of crystallinity appears to be attributed to the modification of the PP matrix in the glass/PP composite studied. The similar crystalline phase content, larger spherulite size and higher dissolution of the interspherulitic regions during etching in the SC condition indicate that the amorphous phase is more concentrated in the regions between individual spherulites than in the NM condition. This is in agreement with previous studies (1,3) showing that the amorphous phase is more concentrated between spherulites for slow cooling conditions and that wetting of the fiber surface is more pronounced for rapid cooling conditions due to the enhanced entrapment of tie molecules and amorphous phase within spherulites.

The high crystalline phase content in the LTM condition also indicates that the original crystalline structure of the glass/PP tapes was not completely destroyed due to the low molding temperature employed (163°C) compared to the thermodynamic melting temperature of PP of 170-180°C (3). Thus, the crystallization in the latter originated from the crystallites still present in the melt. In this condition, highly heterogeneous crystallization coupled with low viscosity of the PP matrix and rapid cooling resulted in a relatively high degree of crystallinity, a very fine crystalline structure and poor fiber dispersion.

Mechanical Behavior

The three-point bending results and SBS results as well as Young's modulus of the glass/PP composites in the three molding conditions are reported in Table 3. The molding conditions significantly affects the flexural properties measured. The maximum strain at the outer fibers, not reported in table 3, remains constant at approximately 2% since, in unidirectional glass composites, it is more dependent on the maximum elongation of the glass fibers, which is not affected by the molding conditions. As shown in Table 3, the highest results are obtained in the NM condition. In the SC condition, a lower flexural strength, a slightly lower interlaminar shear strength and improved Young's and flexural moduli are obtained in comparison with the NM condition. The latter effects can be attributed to the larger spherulites obtained in the SC conditions, separated by higher amounts of the soft amorphous PP phase. The very high interlaminar shear strength values, obtained at –40°C, are in agreement with the maximum shear strength of pure PP generally reported at this temperature. In the LTM condition, a lower flexural strength, a considerably lower interlaminar shear strength and improved Young's and flexural moduli are obtained in comparison with the NM condition. In the LTM condition, the increased crystallinity and very fine crystalline structure probably accounts for the increased moduli obtained; whereas, the low values of interlaminar shear strength can be attributed to the poor fiber dispersion. These results indicate that, in all conditions tested, the composites obtained are properly consolidated and that their mechanical performance, in terms of SBS, three-point bending and tensile tests, are acceptable.

Mode II Interlaminar Crack Propagation

Compliance Calibration

The compliance calibration of the glass/PP composites in the three molding conditions was performed in monotonic and cyclic loading conditions. In Fig. 5, the experimentally determined compliances are compared with the theoretical values predicted from Eq. 2. Excellent agreement between the experimental and calculated values of compliance is obtained. It is therefore assumed that the crack length can be monitored with the compliance calibration method during mode II interlaminar fracture and fatigue testing to obtain the subcritical crack propagation and the fatigue crack propagation curve of glass/PP composite, as earlier stated (11,12,).

Fracture Resistance

An example of the load-deflection curves of the glass/PP composite is presented in Fig. 6 for each of the molding conditions tested. As shown by these curves, some subcritical crack propagation, the amount of which depended on the molding conditions employed, preceded crack instability. These results indicate that the molding conditions greatly influence the fracture resistance of this composite. The $G_{IIc,subcritical}$ values, determined from the point of deviation from the linear portion of the load-deflection curve (indicated in Fig. 6 by arrows), and the $G_{IIc,instability}$ values, determined from the maximum load on the load-deflection curve, are reported in Table 4. The NM condition shows the highest fracture resistance for the molding conditions tested. The $G_{IIc,subcritical}$ value is 2600 J/m^2 and G_{IIc} then increases by a factor of 2.3 to the maximum ($G_{IIc,instability}$) value of 5900 J/m^2. In the SC condition, $G_{IIc,subcritical}$ is 1000 J/m^2 and G_{IIc} then increases by a factor of only 1.1 to the maximum ($G_{IIc,instability}$) value of 1100 J/m^2. In the LTM condition, $G_{IIc,subcritical}$ is 1200 J/m^2 and G_{IIc} then increases by a factor of 1.7 to the maximum ($G_{IIc,instability}$) value of 2000 J/m^2.

The results presented in Fig. 6 and Table 4 indicate that, as the subcritical crack propagates, the increase in the strain energy required for additional propagation depends on the molding condition. To understand the effect of the molding conditions on G_{IIc} at the onset of subcritical crack propagation and during subsequent crack instability, detailed fractographic observations were performed. SEM observations of the mode II interlaminar fracture surfaces of the glass/PP composite are shown in Figs. 7-9. Two typical fractographs are presented for each molding condition, one at the onset of subcritical crack propagation and the other after or near the crack instability. Specific features of the latter observations are shown at higher magnification. The crack propagation direction is from left to right in all fractographs presented in this paper.

The predominant fracture surface features observed for the composites processed under the NM condition are shown in Fig. 7. The fracture surface is covered with a large number of glass fibers (Figs. 7a and b), some of which became detached from the matrix and subsequently fractured. The matrix fracture is transpherulitic with indications of important plastic shearing visible. As the crack propagates, the amount of matrix shearing increases significantly (Fig. 7b). At higher magnification (Fig. 7c), U-shaped half-dimples, typical of shear fracture (15), can be observed

in the fiber imprints (the depressions left by the fibers removed from the observed crack face). Important shearing of the matrix attached to a fiber can also be observed.

The predominant fracture surface features observed for the composites processed under the SC condition are shown in Fig. 8. The fracture is interspherulitic at the onset of subcritical crack propagation (Fig. 8a). The latter surface shows some signs of damage induced by the crack faces rubbing together. As the crack propagates (Fig. 8b), fibers, at times broken and detached, are occasionally observed on the fracture surface. When present, these fibers show signs of associated shearing of the matrix (Fig. 8b) attached to the fibers. At higher magnification (Fig. 8c), significant stretching (mode I fracture), shearing (mode II fracture) and rubbing damage can be observed on the spherulite faces, with the type of damage observed influenced by the orientation of these faces. When not parallel to the average crack plane and in the crack propagation direction, the spherulite faces show important stretching. When close to parallel to the average crack plane, the spherulite faces show extensive shearing. When they are not parallel to the average crack plane and face the direction opposite that of crack propagation, the spherulite faces show rubbing damage. Examples of these features are presented in Fig. 8c. In agreement with the observations for the NM condition (Fig. 7), the presence of fibers on the fracture surface for the SC condition is associated with matrix shearing (Fig. 8b) close to the fiber-matrix interface.

The predominant fracture surface features observed for the composites processed under the LTM condition are shown in Fig. 9. The fracture surface (Fig. 9a) is covered with a large number of glass fibers and the matrix fracture is transpherulitic, similar to that observed for the NM condition (Fig. 7); however, with less shearing of the matrix and more fibers visible on the fracture surface. Fibers detached from this surface and indications of matrix shearing are also increasingly observed as the crack propagates (Fig. 9b). Qualitatively, the same fractographic features are observed for the NM and LTM conditions.

The fractographic observations as well as the load-deflection curves obtained indicate that mode II interlaminar crack propagation under monotonic loading in the glass/PP composites studied includes the following events. When the amorphous phase is uniformly dispersed throughout the matrix and a fine distribution of spherulite is present (NM condition), subcritical crack propagation starts under shear loading in the matrix by void coalescence very close to the fiber-matrix interface. The presence of U-shaped half-dimples indicates that these voids are initiated in

front of the crack tip, as a result of the stress concentration at the fiber-matrix interface. Once initiated at this interface, the main crack can jump into secondary cracks formed in the plastic zone at other fiber-matrix interfaces. This crack jumping leaves glass fibers attached to both crack sides. As both sides of the crack move apart in shear due to the deflection of the ENF specimen, the latter fibers are progressively loaded in uniaxial tension, leading eventually to their fracture. This effect, which has been referred to as fiber nesting (2), is responsible for an important part of the increase in G_{IIc} indicated by the load-deflection curves (Fig. 6) and for the corresponding very high $G_{IIc,instability}$ value. This fiber effect also results in shear loading of the matrix attached to the fibers. Such important shearing of the matrix may be also responsible for a minor part of the increase in G_{IIc} observed on the load-deflection curves (Fig. 6). A schematic representation of these events is shown in Fig. 10.

When the amorphous phase is more concentrated between spherulites and has a coarser distribution (SC condition), crack propagation starts between spherulites at a comparatively lower $G_{IIc,subcritical}$ value than for the NM condition, in agreement with the flexural results obtained (Table 3). The low mechanical resistance of the composite processed under the SC condition is attributed to the weaker interspherulitic regions resulting from the low cooling rate, in agreement with the concentration of soft amorphous phase in the interspherulitic regions observed. In this condition, the fractographic observations show that crack propagation between spherulites occurs under shear loading, with some rubbing due to friction between the crack faces and some stretching of the matrix also observed. Since the soft amorphous PP phase is more concentrated in the interspherulitic regions for the SC condition, fiber nesting occurs only when secondary cracks form in the interspherulitic regions close to a glass fiber. The crack instability for this interspherulitic crack propagation thus occurs rapidly after the subcritical crack propagation (Fig. 6). When observed, fiber nesting results in shear loading of the matrix attached to the fibers. This indicates that, while the amorphous phase is more concentrated at the fiber-matrix interface for the NM condition, the fiber-matrix adhesion remains relatively high for the SC condition. A schematic representation of these events is shown in Fig. 10.

The fracture surface observations for the LTM condition show that crack propagation was quite similar to that for the NM condition. This crack propagation also occurs under shear loading in the matrix very close to the fiber-matrix interface, but with a considerably lower $G_{IIc,subcritical}$ value than for the NM condition. This is in

agreement with the low interlaminar shear strength obtained for the LTM condition (Table 3). This low mechanical resistance for this condition is attributed to the poor fiber dispersion that results from the low molding temperature. Crack jumping associated with weaker fiber-matrix interfaces results in fiber nesting and matrix shearing for the LTM condition. Both of the latter effects contribute to the increase in G_{IIc} during subcritical crack propagation (Fig. 6) for this condition.

Since crack propagation occurs mainly in the softer amorphous phase, the distribution of which depends on the cooling conditions, $G_{IIc,subcritical}$ quantifies the fracture resistance of the fiber-matrix interface for the NM and LTM conditions, while it quantifies the fracture resistance of the interspherulitic regions for the SC condition. The difference between $G_{IIc,instability}$ and $G_{IIc,subcritical}$ is however more indicative of the contribution of fiber nesting and of matrix shearing to the crack propagation resistance under different molding conditions. The crack propagation results and fractographic observations presented indicate that the mode II interlaminar fracture of the glass/PP composite studied is controlled by the matrix, the fiber-matrix interface and the fibers, all of which are affected by the molding conditions. Contrary to the flexural test results (Table 3), which suggest a minor influence of the cooling rate on the mechanical performance of the composite studied, the fracture results demonstrate that the cooling rate and the molding temperature are important. These results differ from those on other glass/PP composites (2), which suggested that the mode II interlaminar fracture tests were considerably less sensitive than mode I interlaminar fracture tests. Moreover, the fracture resistance presently obtained for the NM condition is significantly higher than that reported for other glass/PP composites (2). This can be attributed to the improvements in fiber-matrix adhesion for the glass/PP composite studied as a result of the formulation of the PP matrix. This is in agreement with the high interlaminar shear strength obtained (Table 3), even when taking into account that it was obtained at –40°C, compared with the limited single fiber pull-out values of 5 to 9 MPa reported for other glass/PP composites (2).

As mentioned previously, the fractographic observations reveal the presence of U-shaped half-dimples and important shearing of the matrix attached to the fibers, indicating that shear-related crack propagation is obtained using ENF specimens of the glass/PP composite. It is thus concluded that the $G_{IIc,subcritical}$ results obtained reflect the mode II interlaminar fracture resistance at the onset of subcritical crack propagation of the glass/PP composite

studied. This conclusion differs from that of a previous study (16), based mainly on fractographic observations of brittle composites, such as glass/epoxy or graphite/epoxy, in which it is stated that the fracture in mode II loading using ENF specimens actually results from tension failures in front of the crack tip and not from the sliding of two planes relative to one another. The fractographic features presented in that study (16) differed significantly from those observed in the present study. These differences may be attributed to the ductile nature of the PP matrix in the present composite.

Fatigue Resistance

The mode II interlaminar fatigue crack propagation curves of the glass/PP composite are shown in Fig. 11. While significant scatter in the test data was obtained, these fatigue propagation curves nevertheless clearly indicate that the molding conditions greatly affect the mode II interlaminar fatigue crack propagation behavior of the glass/PP composites. The fatigue propagation curves in Fig. 11 also show the constant power-law behavior or Paris regime (17), given in terms of ΔG_{II}, by:

$$\frac{da}{dN} = k \cdot \Delta G_{II}^{\,n} \tag{4}$$

where k is the fatigue crack growth rate at ΔG_{II} = 1 J/m^2 and n is the slope on the curve on a log-log scale. The values of k and n are presented in Table 5. Despite the large effect of the molding conditions on the fatigue crack propagation curves presented in Fig. 11, the values of the n-exponent only vary between 4.3 and 4.8. These values of n compare well with the Paris regime exponent of 4.4 reported for mode II interlaminar fatigue crack propagation in unidirectional carbon fiber/polyetheretherketone (CF/PEEK) composites (11,12).

Similar to the fracture resistance results, the results in Fig. 11 show that the highest resistance to fatigue propagation is obtained for the NM condition. However, the resistance to mode II interlaminar fatigue propagation is superior for the SC condition than for the LTM condition, contrary to the results obtained in mode II interlaminar fracture. As shown in Table 5, the fatigue crack growth rates at a given value of ΔG_{II} are one decade higher for the SC condition and two decades higher for the LTM condition than those obtained for the NM condition. The mode II fatigue crack propagation results rank in the same order as the interlaminar shear strength results presented in Table 3. The fact that mode II interlaminar fracture results show a superior resistance to crack propagation for the LTM condition than

for the SC condition, while the mode II interlaminar fatigue results show higher fatigue crack growth rates for the LTM condition than for the SC condition is by no means a contradiction. The former material property relates to the intrinsic resistance to steady crack propagation of a given composite; whereas, the latter property relates to the fatigue crack growth rate at a given cyclic loading level (strain energy), considerably lower than the level at which steady crack propagation occurs.

From these results, it is evident that the mode II interlaminar fatigue behavior is very sensitive to the morphology and microstructure of the glass/PP composite resulting from the molding conditions. G_{IIc} values reported for other glass/PP composites (2) are similar to the ΔG_{II} values presently obtained for fatigue crack growth rates of 10^{-6} to 10^{-5} mm/cycles, depending on the molding condition considered. Thus, the glass/PP composites tested are significantly more resistant to mode II interlaminar fatigue and fracture than those studied previously (2). SEM observations of the mode II interlaminar fatigue surfaces of the glass/PP composites are shown in Figs. 12-14. Specific features of the fractographic observations are discussed.

The predominant fatigue surface features observed for the composites processed under the NM condition are shown in Fig. 12. The fatigue surface presents a large number of glass fibers or glass fiber imprints (Fig. 12a). The matrix fracture is transpherulitic, with regularly spaced shear cusps covering most of the fatigue surface. At higher magnification, the matrix shear cusps appear damaged by the cyclic sliding of the crack faces (Fig. 12b). The presence of debris in the latter, which probably corresponds to plastically-rolled matrix from damaged ends of shear cusps, is also noted. The size of and the distance between such cusps increase as the fatigue crack growth rates is observed to increase. They also become considerably less damaged with increasing crack growth rate, with less debris noted on the fatigue fracture surface. These cusps are mostly present in the matrix between fibers or in fiber imprints. However, some cusps can be observed in the matrix covering the fibers (Fig. 12c), indicating that cusps also form at the fiber-matrix interface. A very large number of sheared matrix ligaments are also present at the fiber-matrix interface in the latter, indicative of matrix shearing as a result of the shear stress transfer between the fiber and the matrix.

The predominant fatigue surface features observed for the composites processed under the SC condition are shown in Fig. 13. The fatigue crack propagation is almost exclusively interspherulitic (Figs. 13a and b), with an occasional fiber present on the fatigue surface. Rubbing damage is observed over the entire fatigue surface. When present, the fibers showed signs of associated matrix shearing (Fig. 13a). At higher magnification (Fig. 13b), significant amounts of matrix shearing (mode II), shear cusps and rubbing damage can be observed on the spherulite faces depending on their orientation, similar to the fracture surface observations. A large region parallel to the average crack plane, approximately 65 μm in diameter, probably corresponding to one or a few large spherulites formed between two closely spaced fibers (distance between fibers ≈ 65 μm), is shown in Fig. 13c. Shear cusps also cover the spherulite surface. Larger cusps are observed at the periphery of these crystalline entities.

The predominant fatigue surface features observed for the composites processed under the LTM condition are shown in Fig. 14. The fatigue surface (Figs. 14a and b) presents a large number of glass fibers or glass fiber imprints, as a result of the low fiber dispersion obtained. The matrix fracture is mainly transpherulitic with regularly separated shear cusps present, similar to the observations for the NM condition. Also as for the NM condition, the shear cusps tend to increase in size with the amount of crack propagation. These cusps are mainly present in the matrix between glass fibers or in the glass fiber imprints. The fatigue surface for the LTM condition is thus similar to that for the NM condition. However, regions similar to the interspherulitic regions observed for the SC condition were at times observed on the fatigue surface (bottom of Fig. 14a). The approximately 10-μm diameter of these regions is in agreement with that of the visible crystalline phase observed for the LTM condition mentioned previously. As for the SC condition, these regions of the fatigue surface are covered with shear cusps.

From these fractographic observations as well as from the fatigue crack propagation curves, it is deduced that mode II interlaminar fatigue crack propagation in glass/PP composite involves the following events. When the amorphous phase is uniformly dispersed throughout the matrix with a fine spherulite distribution (NM condition), crack propagation occurs under cyclic shear loading in the matrix at the fiber-matrix interface, as indicated by the presence of remnants of cusps covering the fibers and in the fiber imprints. These cusps initiated in the plastic deformation zone in front of the crack tip by the formation of sub-critical shear defects under mode II loading (15). Crack propagation thus occurs under cyclic shear loading in the matrix very close to the fiber-matrix interface by the initiation, growth and coalescence of cusps. These cusps in the matrix covering the fibers as well as between the

fibers are partially destroyed due to the sliding action between the crack faces. Once formed at the fiber-matrix interface, the shear cusps extend into the matrix close to the fibers. Their size in the matrix is considerably larger than at the fiber-matrix interface since the shear modulus in the matrix is very low compared to that of the fiber. As the cyclic shear amplitude increases during crack propagation, the cusp size in the matrix tends to increase, in agreement with the supposition that these cusps are the result of plastic deformation in front of the crack tip. Fiber nesting, resulting from the crack jumping into secondary cracks at other fiber-matrix interfaces in the plastic zone, is also observed during fatigue crack propagation, however to a far lesser extent than for crack propagation under monotonic loading. Fiber nesting should thus contribute only slightly to the fatigue crack propagation resistance. This is in agreement with the smaller plastic zone produced in fatigue ($\Delta G_{II} < G_{IIc}$). Consequently, damage accumulation in the plastic zone is more localized at individual fiber-matrix interfaces in cyclic loading than in monotonic loading. The crack propagation events observed in the NM condition during fatigue crack propagation are thus very similar to those observed during monotonic crack propagation (Fig. 10).

When the amorphous phase is more concentrated between more coarsely distributed spherulites (SC condition), some apparent differences from those mentioned above are observed fractographically. In this case, the fatigue propagation is interspherulitic and this propagation meets considerably lower resistance than for the NM condition, in agreement with the mode II fracture results. As for the NM condition, cusp formation is observed for the SC condition but is limited to the interspherulitic regions, contrary to the NM condition for which its formation is observed throughout the PP matrix. Similar to the fracture resistance results, the reduction in fatigue resistance can be attributed to localization of the fatigue damage in the weaker interspherulitic regions, resulting from the low cooling rate employed (1-3). This is in agreement with the concentration of the soft amorphous phase in the interspherulitic regions. That the slope of the fatigue crack propagation curve is similar for both conditions is an indication that the same mechanisms are involved. The fractographic observations suggest that this basic mechanism is cusp formation.

In the LTM condition, the fatigue surfaces are very similar to those observed for the NM condition. Crack propagation also occurs under cyclic shear loading in the matrix very close to the fiber-matrix interface by the initiation, growth and coalescence of cusps; however, the fatigue crack growth rate is considerably higher at a given ΔG_{II} than for the NM condition, in agreement with the mode II fracture results. As concluded previously, the

reduction in fatigue crack propagation resistance in the LTM condition is attributed to the poor fiber dispersion resulting from the low molding temperature employed. Crack propagation can also occur by cusp formation in regions between crystallites, which are located near the average crack plane, resulting locally in fatigue surfaces similar in appearance to the interspherulitic fatigue surfaces observed for the SC condition. The slope of the fatigue crack propagation curve for the LTM condition is similar to that for the NM and SC conditions, indicating that the same crack propagation mechanisms are active for all three conditions.

Cusp Formation

As observed in the NM and the LTM conditions, the size of the cusps formed in the matrix increases as the crack propagates, in agreement with the proposed occurrence of cusp formation (18) in the plastic zone ahead of the crack tip. This observation suggests that the size of the cusps can be related to the plastic zone size, r_p, which under mode II loading of an isotropic body is given by:

$$r_p \approx \frac{3}{2\pi}\frac{\Delta K_{II}^2}{\tau_y^2} \approx \frac{3}{2\pi}\frac{E\,\Delta G_{II}}{\tau_y^2} \tag{5}$$

where ΔK_{II} is the mode II stress intensity factor range and τ_y is the material equivalent yield stress in shear. According to Eq. 5, the size of the cusps should be proportional to ΔG_{II}. The size of the cusps at different ΔG_{II} was therefore measured on the fatigue surfaces. These measurements are plotted *vs.* ΔG_{II} in Fig. 15. Despite the scatter obtained in this figure, presumably associated with the fatigue surface damage complicating the cusp size measurements, it appears that the cusp size increases with increasing ΔG_{II}, proportional to the plastic zone size. These cusps formed in the PP matrix between the glass fibers are thus somewhat similar to the discontinuous growth bands (DGBs) observed in fatigue crack propagation of thermoplastic polymers and blends (19). Further work is required to understand the formation of cups in fatigue of glass/PP composites and to validate the suggested proportionality between the cusp size and ΔG_{II}.

CONCLUSIONS

The crystalline-amorphous phase distribution, fiber distribution, melting temperature and crystallinity of unidirectional glass/PP composites are strongly affected by the molding conditions, but these conditions only produced small variations in the flexural and short-beam shear results. The resistance to mode II interlaminar crack propagation in glass/PP composites, either in cyclic or monotonic loading, was strongly affected by the molding conditions employed and depends mainly on the amorphous/crystalline phase configuration. Crack propagation occurs primarily in the soft amorphous PP phase regions, the distribution of which depends on the molding temperature and the cooling rate. In both monotonic and cyclic loading, crack propagation occurs by the formation, growth and coalescence of shear-associated dimples (cusps).

When a relatively fine spherulitic structure and strong interspherulitic regions are present, crack propagation occurs in the matrix very close to the fiber-matrix interface and the matrix fracture is transpherulitic. As the crack propagates, fiber nesting and associated matrix shearing are also increasingly observed. In this condition, high resistance to mode II interlaminar fracture and fatigue is obtained. When a coarser spherulitic structure and weaker interspherulitic regions are obtained, crack propagation followed the interspherulitic regions with few fibers observed on the crack surface. In this condition, the resistance to mode II interlaminar fracture and fatigue is considerably lower. When a very fine crystalline structure and poor fiber dispersion are obtained, crack propagation also occurs in the matrix very close to the fiber-matrix interface with however considerably more glass fibers visible on the fracture surface. In this condition, the resistance to interlaminar fracture and fatigue is also considerably lower.

In monotonic loading, fiber nesting and associated matrix shearing are related to the significant increase in the mode II interlaminar fracture resistance as the crack propagates. Thus, the $G_{IIc,subcritical}$ values reflect the mode II interlaminar fracture resistance of the glass/PP composite under different molding conditions; whereas, the difference between the $G_{IIc,instability}$ and the $G_{IIc,subcritical}$ values is more indicative of the effect of fiber nesting and matrix shearing on the crack propagation resistance. In cyclic loading, fiber nesting and matrix shearing may also contribute to the increase in fatigue resistance.

Based on fractographic measurements, a linear relationship between the size of cusps and ΔG_{II} is suggested, which indicates that the formation of cusps in fatigue is related to the plastic zone size.

REFERENCES

1. Ye, L., A. Beehag and K. Friedrich. 1995. *Mesostructural Aspects of Interlaminar Fracture in Thermoplastic Composites: Is Crystallinity a Key?* Composites Science and Technology. 53:167-173.
2. Ye, L. and K. Friedrich. 1993. *Interlaminar Fracture (Mode II) of Commingled Yarn-Based GF/PP Composites*. Journal Materials Science. 28:773-780.
3. Youssef, Y. and J. Denault. 1998. *Thermoformed Glass Fiber Reinforced Polypropylene: Microstructure, Mechanical Properties and Residual Stresses.* Polymer Composites. 19:301-309.
4. Bureau, M. N. and J. Denault. 2000. *Fatigue Behavior of Continuous Glass Fiber/Polypropylene composites: Influence of Matrix Nature.* Polymer Composites. 21:636-644.
5. Bureau, M. N., F. Perrin, J. Denault and J. I. Dickson. 2000. *Crack Propagation in Continuous Glass Fiber/Polypropylene Composites: Matrix Microstructure Effect*. Proceedings of ANTEC' 2000 (SPE). 2372-2376.
6. Reifsnider, K. L. 1990. *Damage and Damage Mechanics*. Fatigue of Composite Materials (Reifsnider, K. L., editor). Composite Materials Series, Elsevier. 4:11-77.
7. Talreja, R. 1987. Fatigue of Composite Materials. Lancaster, PA: Technomic Publishing Co., Inc., 181 p.
8. Akshantala, N. V. and R. Talreja. 1998. *A Mechanistic Model for Fatigue Damage Evolution in Composite Laminates*. Mechanics of Materials. 29:123-140.
9. Olley, R. H., D. C. Basset and D. J. Blundell. 1986. *Permanganic Etching of PEEK*. Polymer. 27:344-348.
10. Bu, H., S. Z. D. Cheng and B. Wunderlich. 1988. *Addendum to the Thermal Properties of Polypropylene*. Makromol. Chem. Rapid Comm. 9:75-77.
11. Russell, A. J. and K. N. Street. 1985. *Moisture and Temperature Effects on the Mixed-Mode Delamination Fracture of Unidirectional Graphite/Epoxy*. Delamination and Debonding of Materials. (W. S. Johnson, editor). ASTM STP 876:349-370.
12. Trethewey, B. R., J. W. Gillespie, Jr., and L A. Carlsson. 1988. *Mode II Cyclic Delamination Growth*. Journal of Composite Materials. 22:459-483.

13. Carlsson, L. A., J. W. Gillespie and B. R. Trethewey. 1986. *Mode II Interlaminar Fracture of Graphite/Epoxy and Graphite/PEEK*. Journal of Reinforced Plastics and Composites. 5:170-187.

14. Shultz, J. M. *Microstructural Aspects of Failure in Semicrystalline Polymers*. 1984. Polymer Engineering and Science. 24:770-785.

15. Beachem, C. D. 1965. *Electron Fractographic Studies of Mechanical Fracture Processes in Metals*. Journal of Basic Engineering. Transactions of the ASME. D87:299-306.

16. O'Brien, T. K. 1998. *Composite Interlaminar Shear Fracture Toughness, G_{IIc}: Shear Measurement or Sheer Myth*?. Composite Materials: Fatigue and Fracture (7th ed.). (R. B. Bucinell, editor). ASTM STP 1330:3-18.

17. Paris, P. C. and F. Erdogan. 1963. *A Critical Analysis of Crack Propagation Laws*. Journal of Basic Engineering. Transactions of the ASME. D85:528-534.

18. Purslow, D. 1986. *Matrix Fractography of Fibre-Reinforced Epoxy Composites*. Composites 17:289-303.

19. Bureau, M. N., J. I. Dickson and J. Denault. 1998. *Fatigue Propagation Behaviour of Polystyrene/Polyethylene Blends*. Journal of Materials Science. 33:1405-1419.

Table 1 Description of the molding conditions.

Molding Condition	Molding Temperature (°C)	Holding Time (min)	Cooling Rate (°C/min)
NM	200	5	10
SC	200	5	0.5
LTM	163	20	10

Table 2 Melting temperature at peak of fusion, degree of crystallinity, average and maximum spherulite size of the PP matrix in the glass/PP composite for the NM, SC and LTM conditions.

Molding Condition	Melting Temperature (°C) at Peak of Fusion	Degree of Crystallinity X_c (%)	Average Spherulite Size (μm)	Maximum Spherulite Size (μm)
NM	160.0 ± 0.1	44 ± 5	26	40
SC	162.0 ± 0.1	44 ± 5	34	60
LTM	169.7 ± 0.1	49 ± 5	< 10	≈ 10

Table 3 Mechanical results of the glass/PP composite for the NM, SC and LTM conditions.

Molding Condition	Young's Modulus (GPa)	Flexural Modulus (GPa)	Flexural Strength (MPa)	Interlaminar Shear Strength (MPa)
NM	25.7	24.6	470	51
SC	27.8	25.5	405	47
LTM	29.1	25.6	395	15

Table 4 Values of $G_{IIc,subcritical}$ and $G_{IIc,instability}$ of the glass/PP composite for the NM, SC and LTM conditions.

Molding Condition	$G_{IIc,subcritical}$ (J/m^2)	$G_{IIc,instability}$ (J/m^2)
NM	2600	5900
SC	1000	1100
LTM	1200	2000

Table 5 Values of k and n in Eq. 4 and of da/dN at $\Delta G_{II} = 500\ J/m^2$ of the glass/PP composite for the NM, SC and LTM conditions.

Molding Condition	k value in Eq. 4 (mm/cycle)	n value in Eq. 4	da/dN value at $\Delta G_{II} = 500\ J/m^2$ (mm/cycle)
NM	3.1×10^{-17}	4.3	1.4×10^{-5}
SC	1.1×10^{-16}	4.4	1.0×10^{-4}
LTM	1.0×10^{-16}	4.8	1.1×10^{-3}

FIGURE CAPTIONS

Fig. 1 Schematic representation of the ENF specimen. Symbol P designates the applied load.

Fig. 2 Micrographs of etched pre-polished surfaces of the glass/PP composite in the: a) NM, b) SC and c) LTM conditions.

Fig. 3 Normal distribution of spherulite sizes in the NM and SC condition.

Fig. 4 Endothermic heat flow plotted against temperature from DSC.

Fig. 5 Comparison between the experimental and calculated (Eq. 2) values of compliance during: a) monotonic and b) cyclic loading of the glass/PP composites in the NM, SC and LTM conditions.

Fig. 6 Load-deflection curve of the glass/PP composite obtained for the NM, SC and LTM conditions. The arrows indicate the onset of subcritical crack propagation. Crack instability is taken to occur at the maximum load.

Fig. 7 Mode II interlaminar fracture micrographs for the NM condition: a) at the onset of subcritical crack propagation ($\Delta a \approx 0$ mm); b) after crack instability ($\Delta a = 12.4$ mm); c) near the crack instability ($\Delta a = 6.4$ mm). U-shaped dimples (U), matrix shearing (II) and detached fiber (F) are indicated. The crack propagation direction is from left to right in all fractographs presented in the present paper.

Fig. 8 Mode II interlaminar fractographs for the SC condition: a) at the onset of subcritical crack propagation ($\Delta a \approx 0$ mm); b) after crack instability ($\Delta a = 11.9$ mm); c) near the crack instability ($\Delta a = 0.2$ mm). Surface rubbing (R), matrix shearing (II) and stretching (I) are indicated.

Fig. 9 Mode II interlaminar fractographs for the LTM condition: a) at the onset of subcritical crack propagation ($\Delta a \approx 0$ mm); b) after crack instability ($\Delta a = 19.5$ mm, $G_{IIc} = 2694$ J/m^2). Matrix shearing (II) and detached fiber (F) are indicated.

Fig. 10 Schematic of transpherulitic and interspherulitic crack propagation in mode II.

Fig. 11 Fatigue crack growth rates (da/dN) plotted against ΔG_{II} for glass/PP composites in the NM, SC and LTM conditions.

Fig. 12 Mode II interlaminar fatigue fractographs for the NM condition: a) low magnification and b) high magnification at low fatigue crack growth rates ($a = 33.7$ mm, $da/dN = 1.1 \times 10^{-5}$ mm/cycle, $\Delta G_{II} = 420$ J/m^2);

c) high magnification at intermediate fatigue crack growth rates (a = 43.3 mm, da/dN = 8.5×10^{-5} mm/cycle, ΔG_{II} = 800 J/m^2). Shear cusps (C) and matrix shearing (II) are indicated.

Fig. 13 Mode II interlaminar fatigue fractographs for the SC condition: a) low magnification and b) high magnification at intermediate fatigue crack growth rates (a = 46.5 mm, da/dN = 1.1×10^{-4} mm/cycle, ΔG_{II} = 500 J/m^2); c) high magnification at high fatigue crack growth rates (a = 51.2 mm, da/dN = 6.0×10^{-4} mm/cycle, ΔG_{II} = 700 J/m^2). Shear cusps (C) and surface rubbing (R) are indicated.

Fig. 14 Mode II interlaminar fatigue fractographs for the LTM condition: a) low magnification and b) high magnification at high fatigue crack growth rates (a = 44.5 mm, da/dN = 9.1×10^{-4} mm/cycle, ΔG_{II} = 500 J/m^2). Shear cusps (C) are indicated.

Fig. 15 Cusp size measurements plotted *vs.* the values of ΔG_{II} for the NM and LTM conditions. The measurements of cusp size are reported with a precision of $\pm$ 1.0 μm; the values of ΔG_{II} are reported with a precision of $\pm$5%.

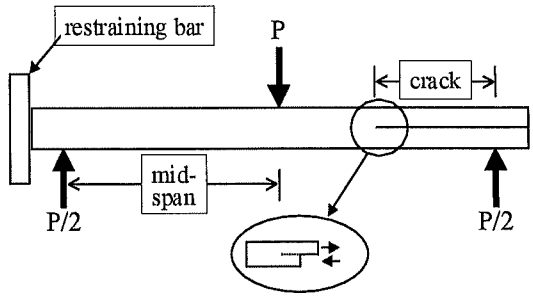

BUREAU *et al.*, Fig. 1

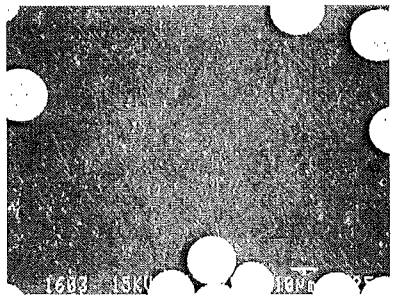

BUREAU *et al.*, Fig. 2a

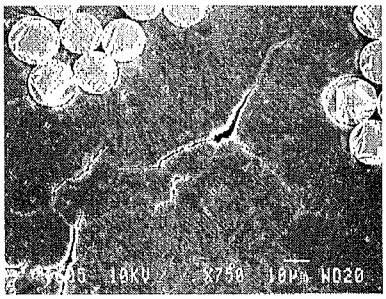

BUREAU *et al.*, Fig. 2b

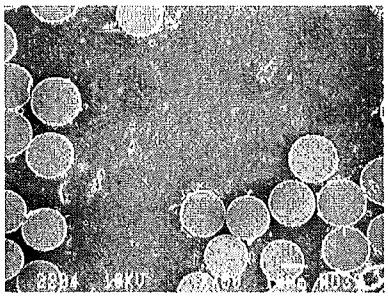

BUREAU *et al.*, Fig. 2c

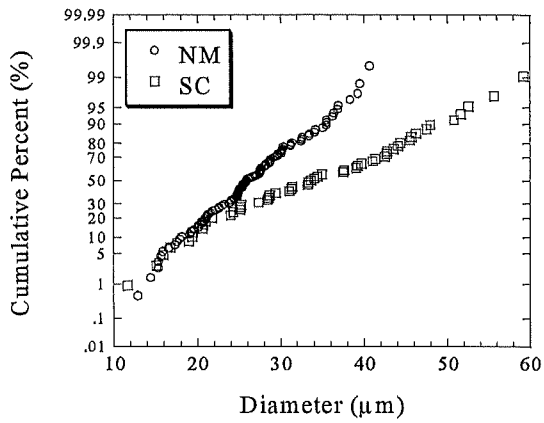

BUREAU *et al.*, Fig. 3

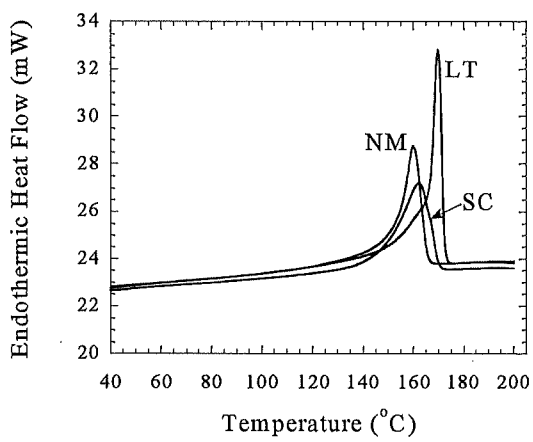

BUREAU *et al.*, Fig. 4

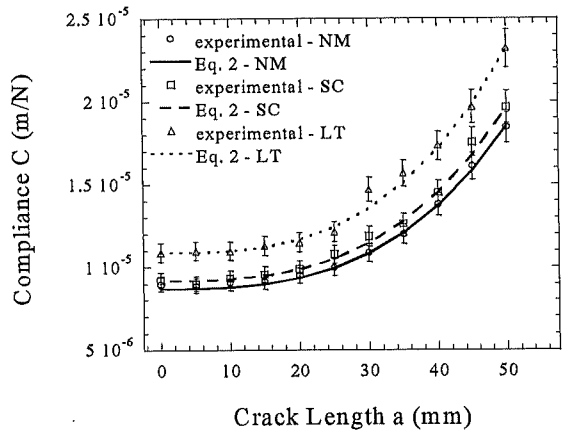

BUREAU *et al.*, Fig. 5a

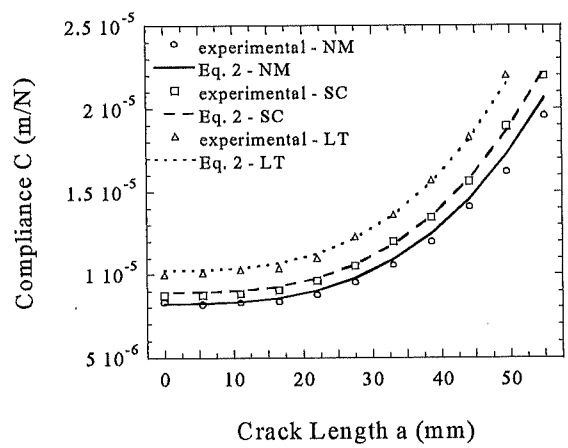

BUREAU *et al.*, Fig. 5b

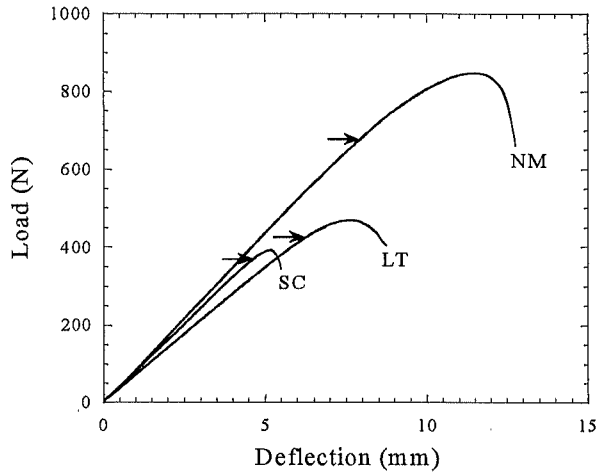

BUREAU *et al.*, Fig. 6

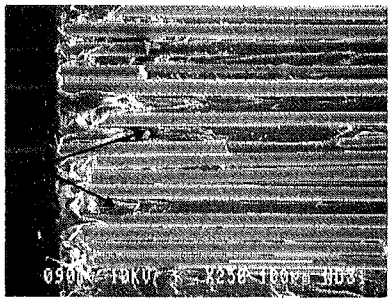

BUREAU *et al.*, Fig. 7a

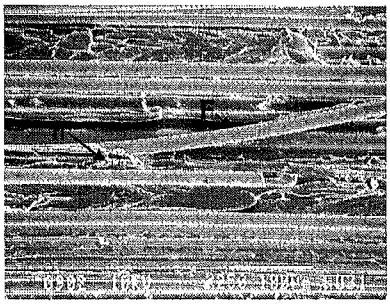

BUREAU *et al.*, Fig. 7b

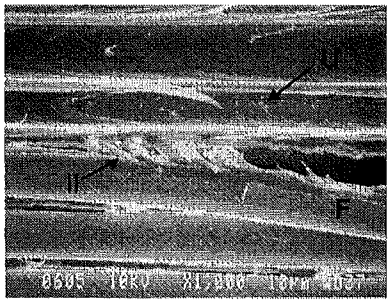

BUREAU *et al.*, Fig. 7c

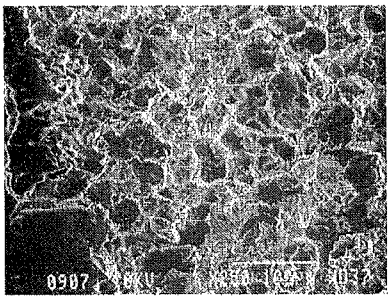

BUREAU *et al.*, Fig. 8a

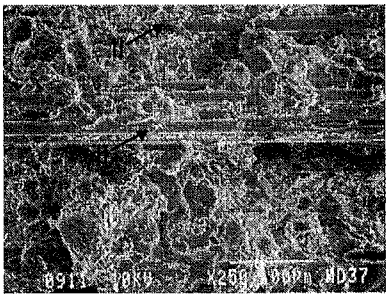

BUREAU *et al.*, Fig. 8b

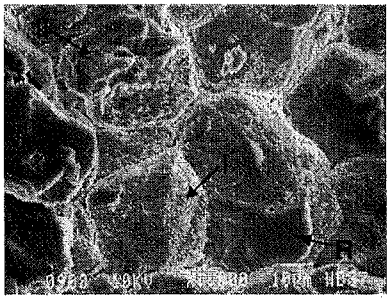

BUREAU *et al.*, Fig. 8c

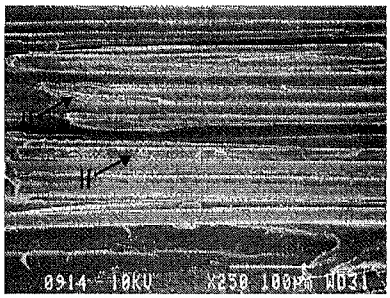

BUREAU *et al.*, Fig. 9a

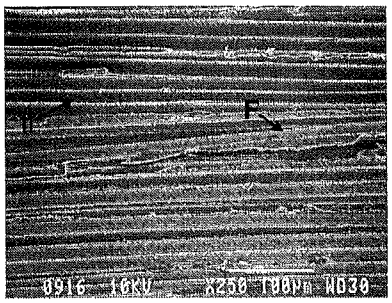

BUREAU *et al.*, Fig. 9b

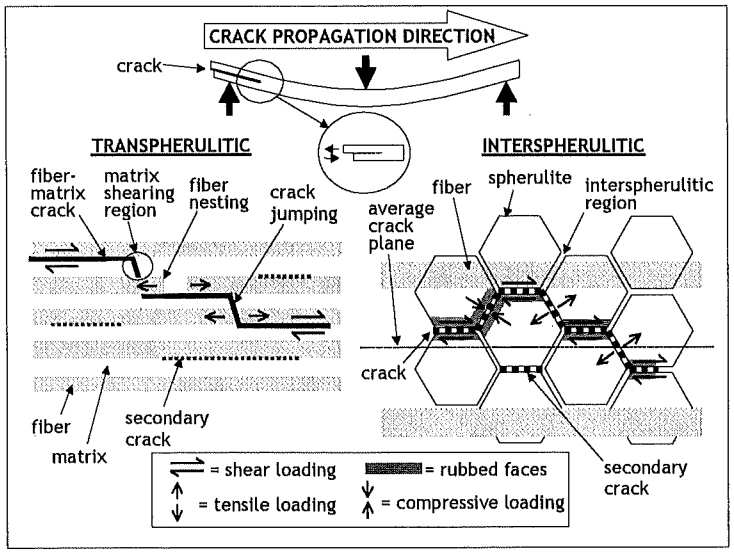

BUREAU *et al.*, Fig. 10

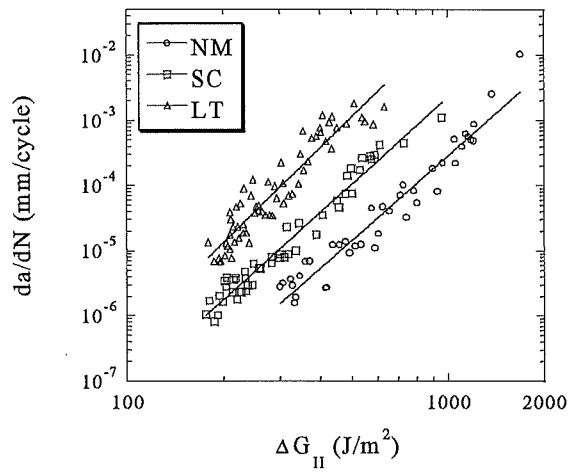

BUREAU *et al.*, Fig. 11

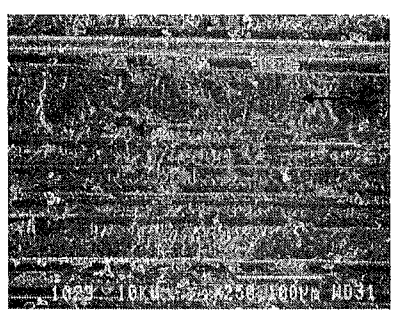

BUREAU *et al.*, Fig. 12a

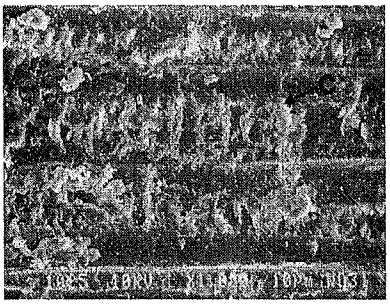

BUREAU *et al.*, Fig. 12b

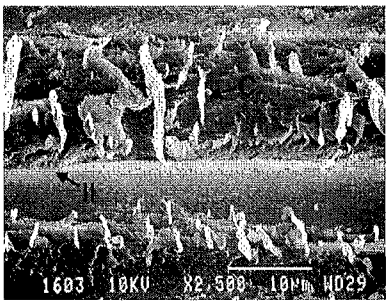

BUREAU *et al.*, Fig. 12c

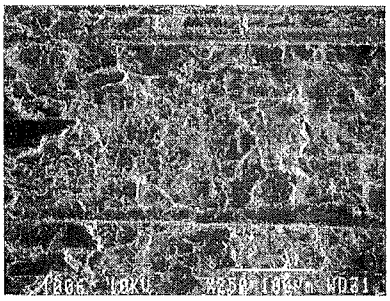

BUREAU *et al.*, Fig. 13a

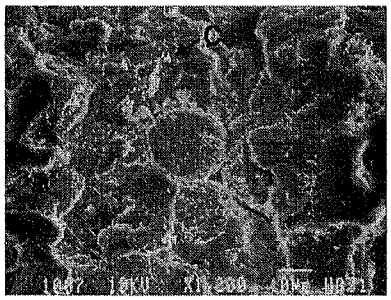

BUREAU *et al.*, Fig. 13b

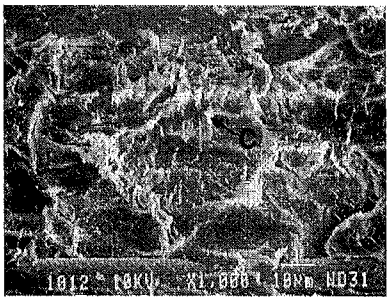

BUREAU *et al.*, Fig. 13c

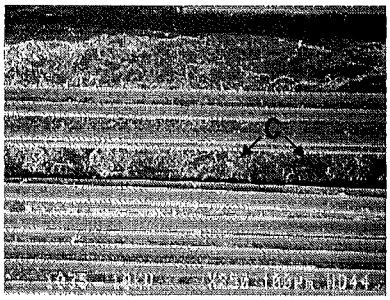

BUREAU *et al.*, Fig. 14a

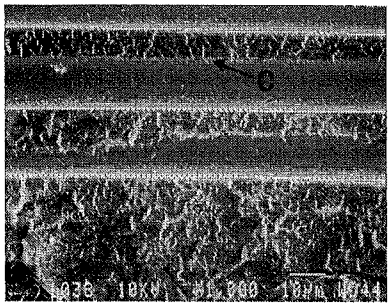

BUREAU *et al.*, Fig. 14b

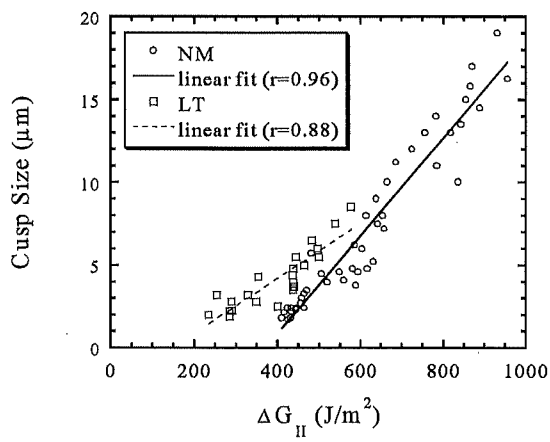

BUREAU *et al.*, Fig. 15